JACS
JOURNAL OF THE AMERICAN CHEMICAL SOCIETY

Communication

pubs.acs.org/JACS

Synergetic Integration of $Cu_{1.94}S–Zn_xCd_{1-x}S$ Heteronanorods for Enhanced Visible-Light-Driven Photocatalytic Hydrogen Production

Yueguang Chen,[†,‡] Shu Zhao,[†] Xian Wang,[∥] Qing Peng,*[,†,‡] Rui Lin,[†,‡] Yu Wang,[†,‡] Rongan Shen,[†,‡] Xing Cao,[†,‡] Libo Zhang,[§] Gang Zhou,*[,§] Jun Li,[†] Andong Xia,[∥] and Yadong Li*[,†,‡]

[†]Department of Chemistry and [‡]Collaborative Innovation Center for Nanomaterial Science and Engineering, Tsinghua University, Beijing 100084, China

[§]State Key Laboratory of Chemical Resource Engineering, Beijing University of Chemical Technology, Beijing 100029, China

[∥]Beijing National Laboratory for Molecular Sciences, Key Laboratory of Photochemistry, Institute of Chemistry, Chinese Academy of Sciences, Beijing 100190, China

Supporting Information

ABSTRACT: In this Communication, we present the integration of synergetic designs into high-quality, well-defined $Cu_{1.94}S–Zn_xCd_{1-x}S$ heteronanorods ($0 \le x \le 1$) for enhanced photocatalytic hydrogen evolution. These heteronanorods possess two light absorbers, intimate heterointerfaces, tunable band gaps over a wide range, and uniform one-dimensional morphology. As verified by experimental and density functional theory studies, these heteronanorods with continuous composition adjustment fully exploit the benefits of both interfacial charge separation and optimized band alignments. Even without any cocatalysts, $Cu_{1.94}S–Zn_{0.23}Cd_{0.77}S$ heteronanorods exhibit efficient hydrogen production activity (7735 μmol h^{-1} g^{-1}) under visible-light irradiation (λ > 420 nm), representing a 59-fold enhancement compared with the pristine CdS catalyst. Meanwhile, deposition of a Pt cocatalyst on the $Cu_{1.94}S–Zn_xCd_{1-x}S$ surface substantially enhances the hydrogen production performance (13 533 μmol h^{-1} g^{-1}) with an apparent quantum efficiency of 26.4% at 420 nm, opening up opportunities to promote the overall photocatalytic performance using rationally designed nanostructures.

Since the discovery of the Honda–Fujishima effect in the early 1970s,[1] photocatalytic hydrogen production through water splitting has become a promising technology for utilizing renewable solar energy.[2−4] Semiconductors, such as CdS-based materials, have emerged as attractive photocatalysts because of their excellent light harvesting, tunable band gaps, and low cost.[5] Because of the giant electron–hole recombination loss, semiconductors are typically modified with metal cocatalysts to extract the electrons for the H^+ reduction reaction.[6,7] Nevertheless, these semiconductor–metal interfaces have yet to become a strong driving force to improve charge collection competitively with the rapid charge recombination.[8] To address this issue, adjusting band gaps to alter light absorption,[9,10] constructing heterojunctions to facilitate spatial charge separation,[11] providing efficient transport pathways,[12] and functionalizing host materials with cocatalysts[13] have been applied to maximize the efficiency of charge utilization. By integration of these design requirements, one-dimensional (1D) semiconductor heteronanorods containing high-crystalline-quality solid solutions may hold a promising potential to synergistically enhance the overall photocatalytic efficiency. However, because of the complexity in the synthesis of multicomponent solid solutions, it is still challenging to achieve tunable band gaps by altering the composition while simultaneously maintaining control over the 1D growth and band-gap alignment of the target heterostructure.

Here we report a highly active visible-light photocatalyst based on monodisperse, single-crystalline, well-defined, 1D $Cu_{1.94}S–Zn_xCd_{1-x}S$ heteronanorods ($0 \le x \le 1$). With continuous composition adjustment, the band gap of $Zn_xCd_{1-x}S$ within the heteronanorod is modified over the entire range (2.57–3.88 eV). Notably, without any metal cocatalyst, $Cu_{1.94}S–Zn_{0.23}Cd_{0.77}S$ heteronanorods achieve an efficient hydrogen production activity of 7735 μmol h^{-1} g^{-1}, a 59-fold enhancement compared with the pristine CdS catalyst. Further decoration with Pt (5 wt %) as a cocatalyst remarkably enhances the hydrogen evolution rate up to 13 533 μmol h^{-1} g^{-1}. As displayed in Figure 1, $Cu_{1.94}S$, a p-type semiconductor with near-infrared (NIR) light absorption, is coupled with visible-light-active $Zn_xCd_{1-x}S$. This combination is expected not only to extend the range of light absorption but also to establish an intimate interface for spatial charge separation. Single-crystalline 1D $Zn_xCd_{1-x}S$ is utilized as an ideal nanostructure for ultrafast charge migration because it contains fewer recombination centers (e.g., grain boundaries or defects) than the polycrystalline material.[14] Thus, our work actualizes the synergetic integration of photocatalytic constituents into a functional heterostructure, providing an effective avenue to optimize the photocatalytic performance by nanoscience techniques.

In a typical synthesis of $Cu_{1.94}S–Zn_xCd_{1-x}S$ heteronanorods, monodisperse $Cu_{1.94}S$ nanospheres were initially prepared as starting materials (see the Supporting Information (SI) for details). Then a mixed precursor of oleic acid (OA), $Zn(Ac)_2·2H_2O$, and $Cd(Ac)_2·2H_2O$ was further introduced for the epitaxial growth of $Zn_xCd_{1-x}S$ (see the SI for details). By varying the Zn to Cd precursor ratio from 0:5 to 2:3, 3:2, 4:1, and 5:0, five

Received: December 4, 2015
Published: March 21, 2016

DOI: 10.1021/jacs.5b12666
J. Am. Chem. Soc. 2016, 138, 4286–4289

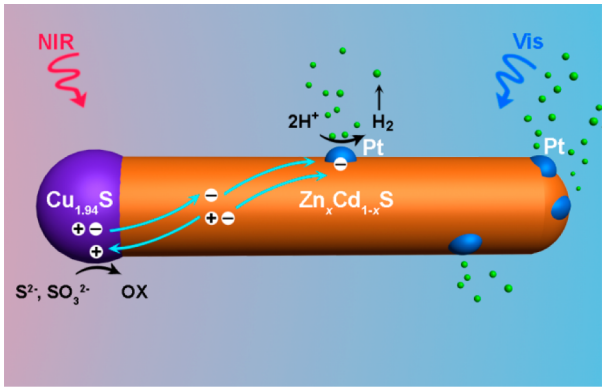

Figure 1. Schematic of the Pt-decorated $Cu_{1.94}S$–$Zn_xCd_{1-x}S$ heteronanorods. $Cu_{1.94}S$ relays the holes from $Zn_xCd_{1-x}S$ to the hole scavengers (S^{2-}, SO_3^{2-}); the electrons are extracted by Pt to transfer rapidly in the single-crystalline 1D structure and eventually diffuse to the surface to carry out water-splitting reactions.

$Cu_{1.94}S$–$Zn_xCd_{1-x}S$ heteronanorods with various compositions were obtained. Figure 2a clearly reveals the uniform, well-defined

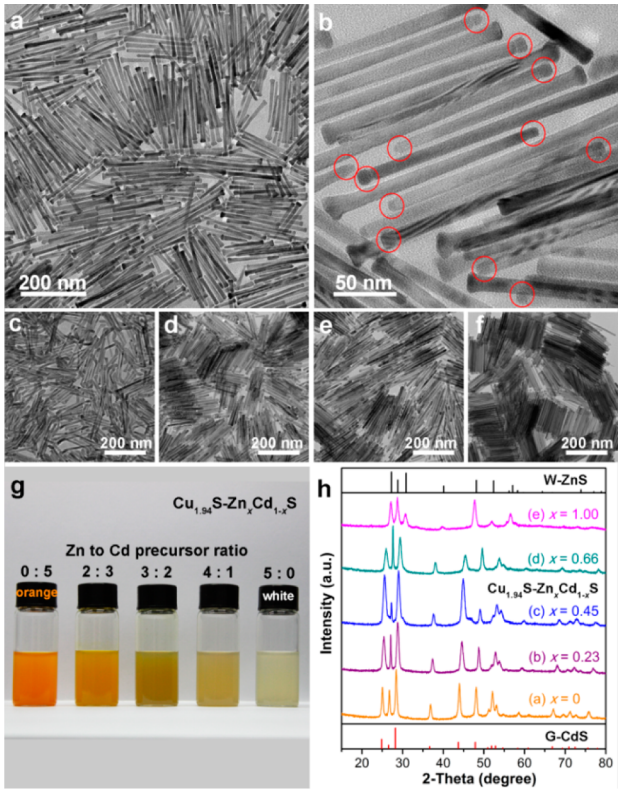

Figure 2. TEM images of $Cu_{1.94}S$–$Zn_xCd_{1-x}S$ heteronanorods prepared with different Zn to Cd molar precursor ratios: (a, b) 2:3; (c) 0:5; (d) 3:2; (e) 4:1; (f) 5:0. The red circles in (b) show $Cu_{1.94}S$ in the corresponding heteronanorods. (g) Color photograph and (h) XRD patterns of the five $Cu_{1.94}S$–$Zn_xCd_{1-x}S$ heteronanorod samples ($0 \leq x \leq 1$). The x values were estimated using Vegard's law.

$Cu_{1.94}S$–$Zn_xCd_{1-x}S$ heteronanorods prepared with a Zn to Cd precursor ratio of 2:3. All of the heteronanorods prepared with different Zn to Cd ratios consist of a semispherical "head" (about 10 nm) and a rodlike "stem" (about 12 nm in diameter and 150–170 nm in length) and possess high size uniformity (Figure 2b–f). With increasing Zn to Cd precursor ratio ($x > 0$), the color of the dispersion of the final products gradually transforms from orange to white (Figure 2g), indicating the composition variation over the whole series of $Cu_{1.94}S$–$Zn_xCd_{1-x}S$ heteronanorods. A contrast experiment performed under the same synthesis conditions but without $Cu_{1.94}S$ nanospheres produced only small $Zn_xCd_{1-x}S$ nanocrystals (Figure S3). Delicate control of synthetic parameters, such as the volume ratio of dodecanethiol and OA, was found to be essential to suppress phase separation and preserve the anisotropic growth of the targeted $Cu_{1.94}S$–$Zn_xCd_{1-x}S$ heteronanorods (Figures S4 and S5).

Apart from the morphology, the crystallographic structure and composition of the heteronanorods were also investigated. When only Cd precursor ($x = 0$) or Zn precursor ($x = 1$) was used as the cation source, the X-ray diffraction (XRD) peaks could be indexed to hexagonal greenockite CdS (JCPDS no. 70-2553) or hexagonal wurtzite ZnS (JCPDS no. 80-0007), respectively (Figure 2h). As the Zn content increased, the XRD peaks of the hexagonal structure shifted continuously toward higher angles over all compositions without phase separation, demonstrating the homogeneous structure of the $Zn_xCd_{1-x}S$ solid solutions within these heteronanorods. The relatively weak diffraction peaks of $Cu_{1.94}S$ could be ascribed to its low content with respect to the entire heteronanorod (Figure 2b). On the basis of Vegard's law, the lattice constant c of $Zn_xCd_{1-x}S$ solid solutions varies linearly with composition. We estimated the x values of the ternary $Zn_xCd_{1-x}S$ according to the c lattice parameters calculated from their diffraction peaks (calculated x = 0.00, 0.23, 0.45, 0.66, and 1.00; Figures 2h and S6).

To gain insight into the formation of these heteronanorods, the microstructures were characterized by high-resolution transmission electron microscopy (HRTEM) and high-angle annular dark-field scanning TEM (HAADF-STEM). The highly crystalline heterointerface in the $Cu_{1.94}S$–$Zn_{0.23}Cd_{0.77}S$ heteronanorods can be clearly seen in Figure 3a. The hexagonal wurtzite $Zn_{0.23}Cd_{0.77}S$ nanorod coherently attaches to the (800) plane of monoclinic $Cu_{1.94}S$ through its (002) plane. Thus, the growth direction of $Zn_{0.23}Cd_{0.77}S$ nanorods is along the [001]

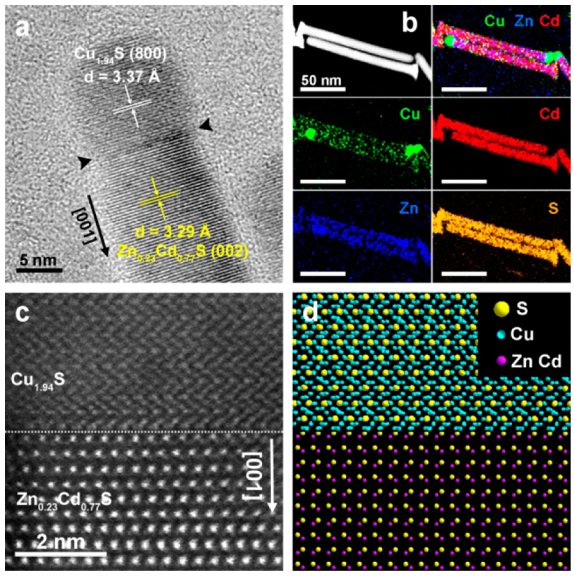

Figure 3. (a) HRTEM and (b) EDX-STEM elemental mapping images of $Cu_{1.94}S$–$Zn_{0.23}Cd_{0.77}S$ heteronanorods. (c) Atomic-resolution aberration-corrected HAADF-STEM image and (d) the corresponding model of the $Cu_{1.94}S$–$Zn_{0.23}Cd_{0.77}S$ heterointerface.

DOI: 10.1021/jacs.5b12666
J. Am. Chem. Soc. 2016, 138, 4286–4289

direction. Similar results were also obtained for the heteronanorods with different compositions (Figure S7). With the increasing x (increasing Zn content), the d spacing of the (002) plane gradually decreases, which is in good agreement with the XRD results. The phenomenon may arise from the substitution of the smaller Zn^{2+} guest ions (0.74 Å) for Cd^{2+} host ions (0.95 Å). The elemental mapping images obtained by energy-dispersive X-ray (EDX)-STEM (Figure 3b) suggest that Cu (green) concentrates at the "head", whereas Zn (blue) and Cd (red) are limited to the stem part and S (yellow) is homogeneously distributed throughout the entire nanorod. The atomic-level HAADF-STEM image and the corresponding structure model of the heterointerface reveal distinct contrast and dissimilar atomic arrangements of the two constituents (Figure 3c,d). The intimate attachment and perfect lattice match of the $Cu_{1.94}S$ (800) and $Zn_xCd_{1-x}S$ (002) planes may dimish the charge transport barriers, thus facilitating ultrafast interfacial charge transfer. The continuous lattice fringes without obvious disorder or defects confirm the high-quality single-crystalline structure of the nanorod (Figure S7e), which is favorable to provide direct and fast charge transport pathways.

The UV−vis−NIR absorption spectra of $Cu_{1.94}S$−$Zn_xCd_{1-x}S$ and $Cu_{1.94}S$ were measured (Figure 4a). $Cu_{1.94}S$ gives a broad

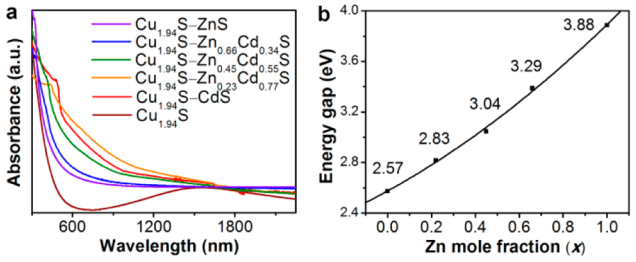

Figure 4. (a) UV−vis−NIR absorption spectra of $Cu_{1.94}S$ seeds and the $Cu_{1.94}S$−$Zn_xCd_{1-x}S$ heteronanorods ($0 \le x \le 1$). (b) Estimated band gaps of $Cu_{1.94}S$−$Zn_xCd_{1-x}S$ as a function of Zn mole fraction.

NIR absorption between 800 and 2300 nm, which is derived from surface plasmon resonances with carrier concentration.[15] Thus, $Cu_{1.94}S$ with its high absorption coefficient can be utilized as an excellent light-harvesting material in solar energy conversion.[16] The $Cu_{1.94}S$−$Zn_xCd_{1-x}S$ heteronanorods with different Zn mole fractions inherit a combination of the band-edge absorption of $Zn_xCd_{1-x}S$ in the UV−vis region and the broad excitonic peaks of $Cu_{1.94}S$ in the NIR region[16] (Figure 4a). With increasing Zn content there is a significant and continuous blue shift (from 482 to 438, 407, 376, and 319 nm) for the $Zn_xCd_{1-x}S$ solid solutions (Figure 4a). The corresponding band-gap energies were estimated from the absorption spectra by the Kubelka−Munk method (Figure 4b).[17] The heteronanorods hold the potential not only to harness more energy in sunlight but also to improve the visible-light functionality through control over the composition, fully exploiting the benefits of the synergetic absorption and band-gap engineering.

The photocatalytic activities for hydrogen evolution of the metal-free $Cu_{1.94}S$−$Zn_xCd_{1-x}S$ heteronanorods ($0 \le x \le 1$) and the corresponding heteronanorods with in situ-photodeposited Pt nanoparticles (NPs) (5 wt %) were evaluated using 50 mL of deionized water containing 0.1 M Na_2S and Na_2SO_3 as hole scavengers under visible-light irradiation ($\lambda > 420$ nm). CdS NPs and $Cu_{1.94}S$ NPs were also examined under identical reaction conditions for comparison (Figures 5 and S10). The results on photocatalytic hydrogen generation clearly demonstrate that the

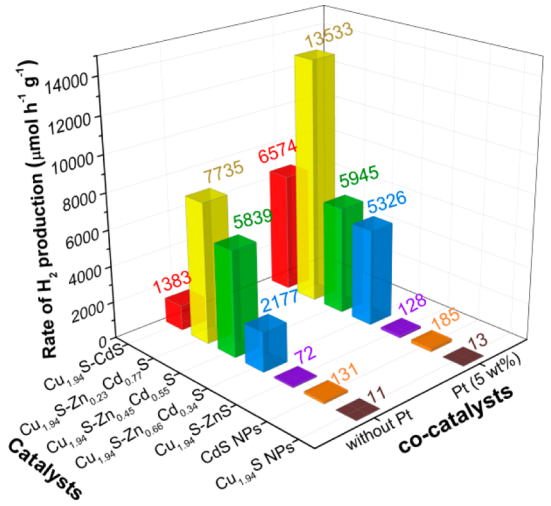

Figure 5. Photocatalytic hydrogen production activities of different samples under visible-light irradiation ($\lambda > 420$ nm).

superior activity of $Cu_{1.94}S$−$Zn_xCd_{1-x}S$ is associated with the formation of the heterostructure as well as the controllable composition. Notably, even without Pt cocatalyst, $Cu_{1.94}S$−$Zn_{0.23}Cd_{0.77}S$ and $Cu_{1.94}S$−CdS heteronanorods achieve H_2 production rates of up to 7735 μmol h^{-1} g^{-1} (corresponding to an apparent quantum efficiency of 8.5% at 420 nm) and 1383 μmol h^{-1} g^{-1}, approximately 59 and 10 times higher that of pristine CdS, respectively (Figure 5). In contrast, both CdS and $Cu_{1.94}S$ samples exhibit low visible-light H_2 production activities, reinforcing the conclusion that the 1D heteronanorod composed of a solid solution and intimate heterojunction is a desired architecture for charge separation and transport. With increasing amount of Zn (from x = 0 to 1), the Pt-decorated $Cu_{1.94}S$−$Zn_xCd_{1-x}S$ heteronanorods show remarkable photoactivity improvement initially and reach a maximum H_2 production rate as high as 13 533 μmol h^{-1} g^{-1} at x = 0.23 with an apparent quantum efficiency of 26.4% at 420 nm; the rate then decreases with further increases in Zn content. This shows that the composition adjustment offers suitable band gaps to substantially boost the photocatalytic performance.

TEM images and XRD analysis verified the successful deposition of Pt NPs (about 15 nm) on the $Cu_{1.94}S$−$Zn_xCd_{1-x}S$ surface after 5 h of irradiation (Figures S11 and S12). No significant shift or decrease of the strong diffraction peaks was observed. This catalyst can retain its good crystallinity and structural stability after the photocatalytic measurement. The results of cycling tests of the visible-light-driven photocatalytic activity of metal-free heteronanorods are illustrated in Figure S12. Even after four consecutive runs without recovery of the catalysts and reagents, our heteronanorod photocatalysts still maintained 70% of the original catalytic activity.

Combining the above with the results of density functional theory (DFT) calculations, we elucidate the potential mechanism from the structural and compositional viewpoints. First, the acceptable lattice mismatch (<6%) and good dangling bond saturation allow the desired interface between $Cu_{1.94}S$ and $Zn_xCd_{1-x}S$ (Figure 6a,b), satisfying the prerequisite for high interfacial charge transfer efficiency. The band alignment (Figure 6c) from the partial density of states (PDOS) (Figure S15) is of type II,[18] realizing the electron−hole spatial separation in $Cu_{1.94}S$/$Zn_{0.23}Cd_{0.77}S$ and $Cu_{1.94}S$/CdS heterojunctions. The carrier dynamics was determined by femtosecond transient

DOI: 10.1021/jacs.5b12666
J. Am. Chem. Soc. 2016, 138, 4286−4289

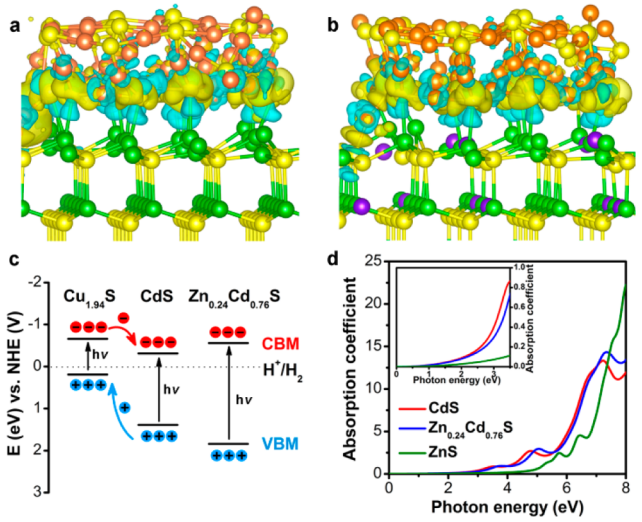

Figure 6. (a, b) Simulated charge distributions at the heterojunction interfaces: (a) $Cu_{1.94}S$/CdS; (b) $Cu_{1.94}S$/$Zn_{0.24}Cd_{0.76}S$. Colors: S, yellow; Cu, orange; Cd, green; Zn, purple. (c) Schematic illustration of the carrier transfer and separation in $Cu_{1.94}S$/$Zn_{0.24}Cd_{0.76}S$ and $Cu_{1.94}S$/CdS heterojunctions from band-edge alignments at the heterointerface based on PDOS. (d) Calculated absorption coefficients of CdS, $Zn_{0.24}Cd_{0.76}S$, and ZnS (the absorption coefficients in the range below 3.5 eV are shown in the inset).

absorption measurements (Figures S16 and S17). Ultrafast hole transfer from $Zn_{0.23}Cd_{0.77}S$ to $Cu_{1.94}S$ with a time constant of around 0.1 ps and electron transfer from $Cu_{1.94}S$ to $Zn_{0.23}Cd_{0.77}S$ with a time constant of about 2.5 ps were observed in the $Cu_{1.94}S$–$Zn_{0.23}Cd_{0.77}S$ heteronanorods upon 400 nm excitation. This further confirms that the efficient carrier separation through the nanojunction occurs. Importantly, the substitution of Zn for Cd increases the band gap of the material. This introduces two effects on the properties of system. The positive contribution arises from the band alignment of the p–n junction. The valence band offset at the interface of $Cu_{1.94}S$–$Zn_{0.23}Cd_{0.77}S$ heterojunctions increases by 0.45 eV compared with that of $Cu_{1.94}S$–CdS ones (Figure 6c). Upon irradiation, the enhanced electric field strength not only speeds up free carriers but also drives more photogenerated holes to transport away from $Zn_{0.23}Cd_{0.77}S$ to $Cu_{1.94}S$ because of the barrier height lowering,[19] thereby further reducing the electron–hole recombination in $Zn_{0.23}Cd_{0.77}S$. On the other hand, relative to CdS, the optical absorption edge of $Zn_{0.23}Cd_{0.77}S$ shows a blue shift of the onset from 2.3 to 2.7 eV, and the absorption coefficient is slightly decreased in the visible-light region (Figure 6d), indicating reductions in the quantum efficiency and the number of available transferred electrons. Consequently, the competition between the two opposite contributions allows optimization of the Zn content to give the best photocatalytic activity. This is in line with our experimental determination of $Zn_{0.23}Cd_{0.77}S$. In addition, the stronger binding energy of Zn–S bonds (−5.08 eV/pair) compared with Cd–S bonds (−4.42 eV/pair) stops the diffusion of Cu atoms crossing the interface,[20] also improving the structural stability and photocatalytic activity of the heterojunctions.

In summary, we have successfully fabricated high-quality $Cu_{1.94}S$–$Zn_xCd_{1-x}S$ heteronanorods ($0 \le x \le 1$) with tunable band gaps over a wide range (2.57–3.88 eV). The synergistic integration endows the heteronanorod photocatalyst with several crucial properties, namely, intense light absorption capability, tunable band gap, efficient spatial charge separation, and swift carrier transport. DFT results preliminarily revealed that $Cu_{1.94}S$ not only contributes to the construction of the intimate heterojunction but also serves as a hole acceptor from $Zn_xCd_{1-x}S$ for spatial charge separation. The composition-dependent activity may stem from the combined effects of the driven force of holes and the available electrons. We hope that this work will open up opportunities for the design and control of multicomponent structures on the nanoscale to inspire the development of innovative catalysts.

■ ASSOCIATED CONTENT

Supporting Information

The Supporting Information is available free of charge on the ACS Publications website at DOI: 10.1021/jacs.5b12666.

Procedures and additional data (PDF)

■ AUTHOR INFORMATION

Corresponding Authors

*pengqing@mail.tsinghua.edu.cn
*gzhou@mail.buct.edu.cn
*ydli@mail.tsinghua.edu.cn

Notes

The authors declare no competing financial interest.

■ ACKNOWLEDGMENTS

We thank the National Natural Science Foundation of China for support (21325101, 21231005, and 21171105).

■ REFERENCES

(1) Fujishima, A.; Honda, K. *Nature* **1972**, *238*, 37.
(2) Turner, J. A. *Science* **2004**, *305*, 972.
(3) Tachibana, Y.; Vayssieres, L.; Durrant, J. R. *Nat. Photonics* **2012**, *6*, 511.
(4) Hisatomi, T.; Kubota, J.; Domen, K. *Chem. Soc. Rev.* **2014**, *43*, 7520.
(5) Chen, J.; Wu, X.-J.; Yin, L.; Li, B.; Hong, X.; Fan, Z.; Chen, B.; Xue, C.; Zhang, H. *Angew. Chem., Int. Ed.* **2015**, *54*, 1210.
(6) Banin, U.; Ben-Shahar, Y.; Vinokurov, K. *Chem. Mater.* **2014**, *26*, 97.
(7) Wu, K.; Zhu, H.; Lian, T. *Acc. Chem. Res.* **2015**, *48*, 851.
(8) Wilker, M. B.; Schnitzenbaumer, K. J.; Dukovic, G. *Isr. J. Chem.* **2012**, *52*, 1002.
(9) Tsuji, I.; Kato, H.; Kobayashi, H.; Kudo, A. *J. Am. Chem. Soc.* **2004**, *126*, 13406.
(10) Maeda, K.; Teramura, K.; Lu, D.; Takata, T.; Saito, N.; Inoue, Y.; Domen, K. *Nature* **2006**, *440*, 295.
(11) Kamat, P. V. *J. Phys. Chem. Lett.* **2012**, *3*, 663.
(12) Warren, S. C.; Voïtchovsky, K.; Dotan, H.; Leroy, C. M.; Cornuz, M.; Stellacci, F.; Hébert, C.; Rothschild, A.; Grätzel, M. *Nat. Mater.* **2013**, *12*, 842.
(13) Zong, X.; Yan, H.; Wu, G.; Ma, G.; Wen, F.; Wang, L.; Li, C. *J. Am. Chem. Soc.* **2008**, *130*, 7176.
(14) Liu, B.; Aydil, E. S. *J. Am. Chem. Soc.* **2009**, *131*, 3985.
(15) Liu, X.; Wang, X.; Zhou, B.; Law, W.-C.; Cartwright, A. N.; Swihart, M. T. *Adv. Funct. Mater.* **2013**, *23*, 1256.
(16) Luther, J. M.; Jain, P. K.; Ewers, T.; Alivisatos, A. P. *Nat. Mater.* **2011**, *10*, 361.
(17) Nowak, M.; Kauch, B.; Szperlich, P. *Rev. Sci. Instrum.* **2009**, *80*, 046107.
(18) Tersoff, J. *Phys. Rev. B: Condens. Matter Mater. Phys.* **1984**, *30*, 4874.
(19) Pau, J. L.; Waters, J.; Rivera, E.; Kim, S. M.; Kung, P. *IEEE Electron Device Lett.* **2015**, *36*, 814.
(20) Jen-La Plante, I.; Teitelboim, A.; Pinkas, I.; Oron, D.; Mokari, T. *J. Phys. Chem. Lett.* **2014**, *5*, 590.

DOI: 10.1021/jacs.5b12666
J. Am. Chem. Soc. 2016, 138, 4286–4289